Ganade, C.E., et al., 2023, Fast exhumation of Earth's earliest ultrahigh-pressure rocks in the West Gondwana orogen, Mali: Geology, https://doi.org/10.1130/G50998.1.

Supplemental Material

Analytical Procedures

Figures S1-S2

Tables S1-S2

1. ANALYTICAL PROCEDURES

1.1. U-Pb geochronology

Zircons and rutile grains were separated from the crushed rock samples using the usual heavy liquid and magnetic techniques. Grains were mounted in epoxy resin and polished down to expose the near-equatorial section. Imaging of zircon grains was acquired at the Research School of Earth Sciences (RSES), at the Australian National University, and at the Geochronological Research Center (CPGeo), at the University of São Paulo (USP). Cathodoluminescence (CL) imaging and inclusion recognition in zircon grains by Energy Dispersive Spectroscopy (EDS) at RSES was done with a JEOL-6610A scanning electron microscope (SEM) supplied with a Robinson detector for cathodoluminescence. Operating conditions for the SEM were 15 kV, 70 mA and a 20 mm working distance. In São Paulo, CL images were obtained using a Quanta 250 FEG SEM prepared with a Centaurus Mono CL3 detector for cathodoluminescence.

Zircon grains were analyzed for U, Th, and Pb in an epoxy mount using the SHRIMP-II at the Research School of Earth Sciences (RSES) at the Australian National University (ANU). SHRIMP conditions and data acquisition were generally as described previously [Williams, 1998]. Each data point was collected in sets of six scans throughout the masses and a reference zircon (TEM2) [Black et al., 2003] was analyzed each fourth analysis. Measured $^{207}Pb/^{206}Pb$ ratios were used for common Pb corrections. The common Pb composition was assumed to be that predicted by the model of Stacey and Kramer [1975]. U-Pb data were collected over three analytical sessions using the same standard, with the different sessions having calibration errors between 1.21% and 2.11% (2-sigma), which was propagated to single analyses. Data evaluation and age calculation were respectively performed in the softwares Squid and Isoplot/Ex [Ludwig, 2009; Ludwig, 2003]. Average $^{206}Pb/^{238}U$ ages are quoted at the 2-sigma confidence level using IsoploR [Vermeesch, 2018].

Rutile grains U-Pb analyses were performed at the Institute of Geological Sciences (University of Bern) using a RESOlution Laser System coupled to an Agilent 7900 quadrupole ICP-MS. A He-H2 gas mixture was used as the aerosol transport gas. Analyses were performed with a laser beam diameter of 40 µm with a 5 Hz frequency and energy densities on the sample 4.0 $J.cm^{-2}$. Sample analyses were calibrated using the primary rutile standard R10 [Luvizotto et al., 2019] and secondary rutile standard R632 [Axelsson et al. 2018] and NIST SRM 610 and 612 [Jochum et al. 2011] were employed to monitor accuracy. Data reduction was performed using the software Iolite [Hellstrom et al. 2008; Paton et al. 2011]. Individual ages for the analysis with neglegible common Pb, concordant in the TW plot, were calculated using IsoplotR (Vermeesch, 2018).

1.2 Zircon and Rutile trace elements

Trace elements in accessory zircon and rutile were analyzed by laser-ablation inductively coupled plasma mass spectrometry (LA-ICP-MS) at RSES. This instrument includes an ANU "HelEx" laser ablation cell [Eggins et al., 1998] built to receive a pulsed 193 nm wavelength ArF Excimer laser with 100 mJ output energy at a repetition rate of 5 Hz and coupled to an Agilent 7500 quadrupole ICPMS. The instrument was tuned for maximum sensitivity and minimum production of molecular species, maintaining ThO+/Th+ at <0.5%. The laser was operated in drilling mode with spot sizes of 28 µm. The total analysis time was 60 s, where the first 25 s of which was background acquisition before ablation. Synthetic glasses (NIST 612 for zircon) were used for external calibration [Jochum, et al., 2011]. The SiO_2 value of 32.45 wt% was used as internal standard for zircon. A secondary natural glass standard (BCR-2) was used to monitor accuracy. Data reduction and evaluation was performed in the software package Iolite v.2.5 and then normalized with the chondrite [Nakamura, 1974] composition.

1.3 Mineral chemistry and quantitative petrological maps

The samples were analyzed by electron probe micro-analyzer (EPMA) using both quantitative spot analyses and X-ray compositional mapping in wavelength-dispersive mode. EPMA analyses were acquired with a JEOL JXA-8200 superprobe at the Institute of Geological Sciences (University of Bern). Conditions for spot analyses were 15 keV accelerating voltage, 10 nA beam current and 40 s dwell times (including 2 × 10 s of background measurement). The following standards were used: almandine (Si, Fe, and Al), forsterite (Mg), orthoclase (K), anorthite (Ca), albite (Na), tephrite (Mn) and ilmenite (Ti) for garnet, and wollastonite (Si), orthoclase (K), anorthite (Al, Ca), albite (Na), forsterite (Mg), almandine (Fe), tephrite (Mn), and ilmenite (Ti) for pyroxene and amphibole. Compositional mapping followed the procedure described in [Lanari et al., 2013] using 15 KeV accelerating voltage, 100 nA beam current and dwell times of 200 ms. Point analyses were measured on the same area and were used as internal standards [De Andrade et al., 2006]. The compositional maps were classified and converted into concentration maps of oxide weight percentage using the software XMapTools 4 (build 220512). Local bulk compositions used in the thermodynamic modelling were approximated from combined oxide weight percentage maps using the export built-in function of XMapTools by integrating the pixel compositions of particular domains after a density correction [Mészaros, et al., 2016; Lanari and Engi, 2017].

1.4 Thermodynamic modeling

The isochemical phase diagrams were computed using the Gibbs free energy minimization THERIAK-DOMINO package (version 04.02.2017) [de Capitani & Brown, 1987; de Capitani & Petrakakis, 2010] using the internally consistent thermodynamic dataset ds55 (update Nov. 2003 of Holland & Powell, 1998). Samples S510, S508, and S520 were modelled in the Na_2O-CaO-K_2O-FeO-MgO-Al_2O_3-SiO_2-TiO_2 chemical system using the local bulk compositions extracted from the X-ray compositional maps. The following mixing models for solid solution were used: garnet, biotite, and melt [White et al., 2007]; white mica [Coggon & Holland, 2002]; ilmenite-hematite [White et al., 2000]; amphiboles [Diener et al., 2007]; clinopyroxene [Diener & Powell, 2012]; feldspars [Holland & Powell, 2003]; epidote, talc, and chlorite [Holland & Powell, 1998]. Pure phases included rutile, titanite,

quartz, Al_2SiO_5 isomorphs and H_2O. The H_2O was set in excess and treated as a perfectly mobile component. Because there is no evidence of partial melting in any of the studied samples, the high-temperature limit of the diagrams is represented by H_2O-saturated *solidus*. MnO and Fe^{3+} were not considered in the models due to negligible spessartine content in garnet, and because all the samples only contain rutile and minor ilmenite as the oxide-bearing phases, which Diener & Powell [2010] showed indicates reducing conditions. The peak P-T conditions were calculated using isopleth interception thermobarometry, considering the maximum and minimum values of interceptions, and the average results are reported at 95% of confidence level. The maximum and minimum intercept values for compositional isopleths were used to calculate the standard error associated with the average peak P-T metamorphic conditions (Figure 2).A minimal absolute error of 50 °C and 0.1 GPa can be assumed for all P-T constraints [Powell & Holland, 2008].

2. Detailed results

2.1 Compositional X-ray maps and mineral chemistry

Sample S508 represents a phengite-rich band of a quartzite, and it is composed of garnet (10.4%), phengite (50.7%), omphacite (27.2%), quartz (2.0%), albite (4.7%), chlorite (3.8%), epidote (0.8%), rutile (0.2%), and apatite (0.1%). Garnet forms aggregates of rounded grains within or at the edges of phengite crystals. Phengite is elongated and defines the lepdoblastic matrix of the rock. Omphacite occurs as prismatic or elongated grains with straight contact against phengite, and embayed contact with garnet, generally replaced by fine-grained symplectites composed of albite + quartz ± Ca-rich pyroxene. Rutile is found as inclusions in garnet, omphacite, and phengite, as well as in interstitial positions among these phases. Epidote and chlorite occur at the symplectite region or along cracks and are interpreted as low-temperature retrograde phases. Garnet and phengite have complex core-rim chemical zoning, whereas omphacite is not zoned. Garnet has a rimward decrease of X_{Prp} content varying from 0.40 to 0.33, with similar, but inverse Ca zoning, with an abrupt transition from X_{Grs}-poor cores of 0.19-0.20 towards the X_{Grs}-rich rims of 0.22-0.26. Phengite shows a rimward decrease

of Si^{+4} *apfu* content, varying from 3.46 at the core to 3.32 at the rim. Omphacite has homogeneous X_{Jd} and X_{Di} contents varying between 0.55-0.61 and 0.32-0.37, respectively.

The mapped area in sample S520 represents a phengite- and garnet-rich band of this quartzite. The main mineralogy is garnet (5.8%), phengite (32.1%), omphacite (13.7%), quartz (31.2%), albite (6.41%), paragonite (2.8%), amphibole (3.31%), kyanite (4.33%), rutile (0.6%), and allanite/apatite/zircon (<0.1%). The main foliation of the rock is marked by the alignment of idioblastic phengite, interstitial quartz, and aggregates of sub-idioblastic omphacite. Garnet is fine-grained and occurs as small, rounded grains included or among contacts between omphacite, phengite, and quartz. Prismatic kyanite occurs within phengite grains and it is replaced at their rims by paragonite. Symplectitic albite + quartz ± amphibole mineral association occurs along the cracks or at the rims of omphacite grains. Rutile occurs as inclusion in garnet, omphacite, phengite, quartz, and kyanite. Calcium carbonate occurs in interstitial sites among garnet, omphacite, phengite, and epidote and it is interpreted as a late retrogressive phase. Contrary to sample S514, garnet in the quartzite sample S520 is less zoned. The X_{Mg} are flat or decrease slightly towards the rim with associated X_{Prp} and X_{Alm} variations from 0.39 to 0.35, and from 0.41 to 0.49, respectively. Garnet also exhibits a subtle increase of X_{Grs} from core to the mantle of 0.17 to 0.21, followed by a depleted outermost rim, with X_{Grs} lower than 0.15. Omphacite is slightly zoned with rimward decrease of X_{Jd} content from 0.62 to 0.40 accompanied by an inverse correlation in the X_{Di} content of 0.34 to 0.40. Phengite shows a rimward decrease of Si^{+4} *apfu* content from 3.44 to 3.28.

Sample S510 corresponds to a garnet-rich portion of the rutile-bearing garnet-omphacite-amphibole eclogite. The main mineralogy of the rock is composed of garnet (44.2%), omphacite (35.4%), quartz (12.8%), amphibole (4.8%), epidote (0.9%), rutile (0.7%), albite (0.5%), paragonite (0.7), and apatite (0.1%). Garnet occurs as a medium to coarse-grained subhedral porphyroblasts containing inclusions of omphacite, rutile, and quartz. The matrix is dominated by coarse-grained omphacite and quartz grains. Amphibole and epidote occur locally overlying the contact of the garnet-omphacite-rutile mineral assemblage, and paragonite occurs as millimeter-sized overgrown flakes after amphibole and/or garnet in the matrix. Garnet in the eclogite sample S510 shows

concentric zoning, with a slight rimward decrease in X_{Grs} and X_{Prp} contents, with values ranging from 0.35 to 0.31 and 0.22 to 0.16, respectively. The clinopyroxene is omphacite and shows a rimward decrease of Na content, with calculated X_{Jd} values ranging from 0.52 to 0.45. Fe and Ca in clinopyroxene have similar zoning, with X_{Hd} values ranging from 0.16 to 0.1.

2.2 Phase equilibrium modelling

For the sample S508, the interpreted peak metamorphic assemblage of garnet-omphacite-coesite/quartz-phengite-rutile-(+kyanite) occurs over a broad *P-T* range of pressure and temperature conditions above the lawsonite- and amphibole-bearing fields. The model predicts the presence of about 1.5% kyanite in equilibrium with the inferred peak metamorphic field, which is a phase not observed in the quantified X-ray map but occurs in other parts of the thin section. The calculated compositional isopleths for the Na- and Si-rich cores of omphacite and phengite intersect, constraining the average P-T conditions of 3.36 ± 0.16 GPa and 743 ± 44 ^{o}C. Under these conditions, the modelled volume of the equilibrium solid phases had good correspondence (difference <4.0 vol.%) with the proportion observed in the quantified X-ray map (**Fig. 3A**). The Ca-Fe-depleted cores of these garnets are interpreted to have formed during prograde metamorphism. This, together with the calculated compositional isopleths for omphacite and phengite rims, suggest a similar prograde/retrograde clockwise *P-T* metamorphic evolution hairpin-style *P-T* path. The retrograde path is also supported by the appearance of amphibole in symplectite after omphacite. The occurrence of amphibole, albite, and epidote as interstitial phases or as symplectites are interpreted as low-temperature retrograde phases.

The inferred peak metamorphic assemblage in sample S520 involves garnet-omphacite-phengite-kyanite-coesite/quartz-rutile and was modelled to be stable at temperatures and pressures greater than 650°C and 2.0 GPa above the amphibole stability field under *sub-solidus* conditions. The Na- and Si-rich cores of the omphacite and phengite, together with the grossular-rich garnet core, were interpreted as having formed in equilibrium during the peak of eclogite-UHP facies metamorphism. The interception of calculated isopleths of the jadeite and grossular molecule, coupled with the Si p.f.u content in phengite, was used to constrain a calculated

average peak metamorphic condition of 3.46 ± 0.14 GPa and 825 ± 34 °C for this sample. The rimward grossular decrease in the small garnet grains, together with the occurrence of retrograde amphibole, epidote, and late paragonite symplectites after kyanite suggests a decompression and cooling *P-T* path up to 670°C and 1.6 GPa. The model also predicted the proportions of solid phases in equilibrium for both peak and retrograde metamorphism with differences of less than 3% compared to that observed in the X-ray compositional map (**Fig. 3B**). However, it should be noted that the calculated amphibole retrograde volume was overestimated by 7% compared to the observed one and the stability of albite was not modelled in the investigated *P-T* window.

For the sample S510, the modelled peak metamorphic assemblage of garnet-omphacite-quartz/coesite-rutile-(+phengite) was calculated to occur at temperatures greater than 600°C and pressures above 2.0 GPa. The model also predicted the stability of 2% phengite due to K_20 present in the bulk rock composition, although this phase was not observed in the X-ray mapped area but was present in nearby eclogites [*e.g.* Ganade et al., 2014]. The intercepts of the isopleths of X_{Jd} in omphacite and the X_{Prp} in the garnet were used to constrain the average P-T conditions of 2.66 ± 0.31 GPa and 725 ± 57 °C for this sample (**Fig. 3C**). The modelled volume for the solid phases in equilibrium at the metamorphic peak had good correspondence with the observed mineral proportion (<5.0 vol.% difference). However, the model overestimated the volume of the retrogressive amphibole and paragonite. The growth of amphibole at the expense of garnet-omphacite-quartz equilibrium assemblage and subsequently crystallization of K-rich mica is consistent with decompression and cooling *P-T* path up to 1.6 GPa at ≈ 620°C. The restricted occurrence of albite and epidote is attributed to late retrograde metamorphism recorded outside of the investigated *P-T* window.

Supplemental figure S1 – *P-T* pseudosections calculated with the local bulk composition of the investigated samples, showing general topologies with isopleth composition, selected mineral proportion (vol%) and density of solids (g/cm^3) modelled along the proposed *P-T* path (indicated by the grey arrow inside the diagram). The star and square symbols indicate the peak *P-T* metamorphic conditions and the retrograde metamorphism

trajectory, respectively. *X*Grs = Ca/(Ca+Fe+Mg) in garnet; *X*Pyp = Mg/(Mg+Fe+Ca) in garnet; *X*Jd = Na/(Na+Ca+Fe+Mg) in clinopyroxene.

Supplemental figure S2 – Energy Dispersive Spectroscopy (EDS) analysis of inclusions of omphacite (A) and garnet (B) in metamorphic zircons from sample S508.

References

Axelsson E., Pape J., Berndt J., Corfu F., Mezger K. and Raith M.M. (2018). Rutile R632 – A new natural reference material for U-Pb and Zr determination. Geostandards and Geoanalytical Research, 42, 319–338.

Black, L. P., Kamo, S. L., Allen, C. M., Aleinikoff, J. N., Davis, D. W., Korsch, R. J., & Foudoulis, C. (2003). TEMORA 1: a new zircon standard for Phanerozoic U–Pb geochronology. Chemical geology, 200(1-2), 155-170.

Coggon, R., & Holland, T. J. B. (2002). Mixing properties of phengitic micas and revised garnet-phengite thermobarometers. Journal of Metamorphic Geology, 20(7), 683-696.

De Andrade, V., Vidal, O., Lewin, E., O'Brien, P. & Agard, P. (2006). Quantification of electron microprobe compositional maps of rock thin sections: an optimized method and examples. Journal of Metamorphic Geology. 24, 655–668.

de Capitani, C. & Brown, T. H. (1987). The computation of chemical equilibrium in complex systems containing nonideal solutions. Geochimica et Cosmochimica Acta. Geochim. Cosmochim. Acta 51, 2639–2652.

de Capitani, C., & Petrakakis, K. (2010). The computation of equilibrium assemblage diagrams with Theriak/Domino software. American mineralogist, 95(7), 1006-1016.

Diener, J. F. A., Powell, R., White, R. W. & Holland, T. J. B. (2007). A new thermodynamic model for clino- and orthoamphiboles in the system Na2OCaO-FeO-MgO-Al2O3-SiO2-H2O-O. Journal of Metamorphic Geology. 25, 631–656.

Diener, J. F. A., & Powell, R. (2010). Influence of ferric iron on the stability of mineral assemblages. Journal of Metamorphic Geology, 28(6), 599-613.

Diener, J. F. A., & Powell, R. (2012). Revised activity–composition models for clinopyroxene and amphibole. Journal of Metamorphic Geology, 30(2), 131-142.

Eggins, S. M., Kinsley, L. P. J. & Shelley, J. M. G. (1998). Deposition and element fractionation processes during atmospheric pressure laser sampling for analysis by ICP-MS. Applied Surface ScienceAppl. Surf. Sci. 129, 278–286.

Ganade, C.E., Rubatto, D., Hermann, J., Cordani, U.G., Caby, R., and Basei, M.A.S., (2014). Ediacaran 2,500-km-long synchronous deep continental subduction in the West Gondwana Orogen: Nature Communications, v. 5, p. 5198, doi:10.1038/ncomms6198.

Green, E. C. R., Holland, T. J. B. & Powell, R. (2007). An order-disorder model for omphacitic pyroxenes in the system jadeite-diopside-hedenbergite-acmite, with applications to eclogite rocks. Am. erican Mineralogists. 92, 1181–1189.

Hellstrom, J., Paton, C., Woodhead, J., & Hergt, J. (2008). Iolite: software for spatially resolved LA-(quad and MC) ICPMS analysis. *Mineralogical Association of Canada short course series*, *40*, 343-348.

Holland, T. J. B. & Powell, R. (1998). An internally consistent thermodynamic data set for phases of petrological interest. Journal of . Metamorph. ic Geology. 16, 309–343.

Holland, T. J. B. & Powell, R. (2003). Activity–composition relations for phases in petrological calculations: an asymmetric multicomponent formulation. Contributions to Mineralogy and Petrology, 145(4), 492-501.

Jochum, K. P., Weis, U., Stoll, B., Kuzmin, D., Yang, Q., Raczek, I., ... & Enzweiler, J. (2011). Determination of reference values for NIST SRM 610–617 glasses following ISO guidelines. Geostandards and Geoanalytical Research, 35(4), 397-429.

Lanari, P., Riel, N., Guillot, S., Vidal, O., Schwartz, S., Pêcher, A., & Hattori, K. H. (2013). Deciphering high-pressure metamorphism in collisional context using microprobe mapping methods: Application to the Stak eclogitic massif (northwest Himalaya). Geology, 41(2), 111-114.

Lanari, P., Giuntoli, F., Loury, C., Burn, M. & Engi, M, (2017). An inverse modeling approach to obtain P-T conditions of metamorphic stages involving garnet growth and resorption. European. J. ournal of Mineralogy. 29, 181–199.

Ludwig, K. R. Isoplot/Ex version 3.0. A Geochronological Toolkit for Microsoft Excel (Berkeley Geochronological Centre, Special Publication, 2003).

Ludwig, K. R. SQUID 2: A User's Manual, Rev (Berkeley Geochronology Center, Special Publication, 2009).

Luvizotto G.L., Zack T., Meyer H.P., Ludwig T., Triebold S., Kronz A., Mu€nker C., Sto€ckli D.F., Prowatke S., Klemme S., Jacob, D.E. and von Eynatten H. (2009). Rutile crystals as potential trace element and isotope mineral standards for microanalysis. Chemical Geology, 261, 346–369.

Mészaros, M. et al. Petrology and geochemistry of feldspathic impact-melt breccia Abar al' Uj 012, the first lunar meteorite from Saudi Arabia. Meteoritics & Planetary ScienceMeteor. Planet. Sci. 51, 1830–1848 (2016).

Nakamura, N., (1974). Determination of REE, Ba, Fe, Mg, Na and K in carbonaceous and ordinary chondrites: Geochimica et Cosmochimica Acta, v. 38, p. 757–775, doi:10.1016/0016-7037(74)90149-5.

Paton, C., Hellstrom, J., Paul, B., Woodhead, J., & Hergt, J. (2011). Iolite: Freeware for the visualisation and processing of mass spectrometric data. Journal of Analytical Atomic Spectrometry, 26(12), 2508-2518.

Powell, R., & Holland, T. J. B. (2008). On thermobarometry. Journal of Metamorphic Geology, 26(2), 155-179.

Stacey, J. S. & Kramer, J. D. (1975). Approximation of terrestrial lead isotope by a two-stage model. Earth Planet. Sci. Lett. 26, 207–212 (1975).

White, R. W., Powell, R. & Holland, T. J. B. (2007). Progress relating to calculation of partial melting equilibria for metapelites. Journal of. Metamorphic. Geology. 25, 511–527 (2007).

White, R. W., Powell, R., Holland, T. J. B., & Worley, B. A. (2000). The effect of TiO2 and Fe2O3 on metapelitic assemblages at greenschist and amphibolite facies conditions: mineral equilibria calculations in the system K2O-FeO-MgO-Al2O3-SiO2-H2O-TiO2-Fe2O3. Journal of Metamorphic Geology, 18(5), 497-511.

Williams, I. S. Application of Microanalytical Techniques to Understanding Mineralizing Processes Vol. 7 (eds. McKibben, M. A. et al.) 1–35 (Reviews in Economic Geology, Society of Economic Geologists, 1998) (2008).

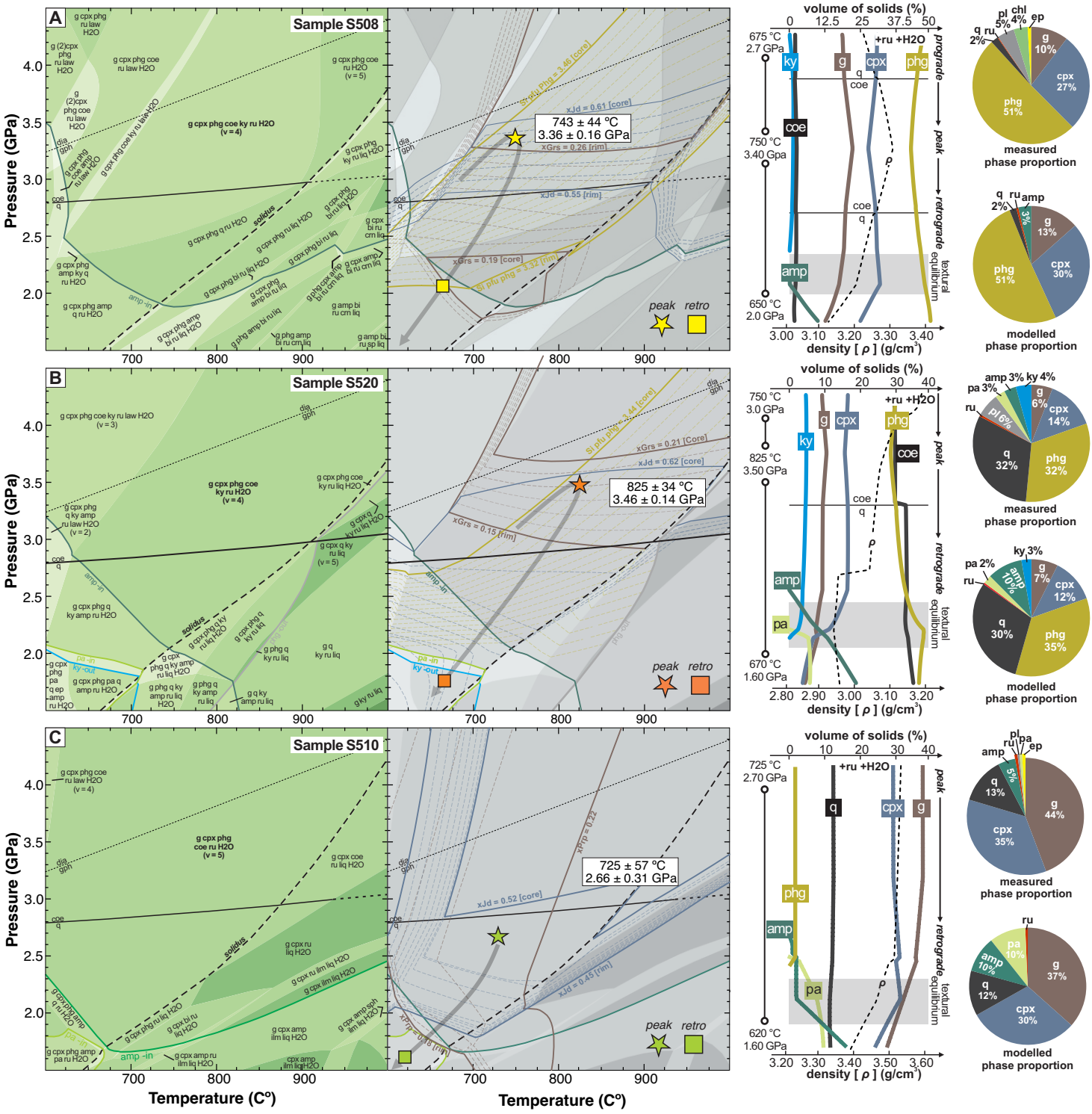
A
Sample S508
B
Sample S520
C
Sample S510
Pressure (GPa)
Temperature (C°)
743 ± 44 °C
3.36 ± 0.16 GPa
825 ± 34 °C
3.46 ± 0.14 GPa
725 ± 57 °C
2.66 ± 0.31 GPa
peak
retro
volume of solids (%)
density [ρ] (g/cm³)
prograde
peak
retrograde
textural equilibrium
+ru +H2O
measured phase proportion
modelled phase proportion

Fig. S1

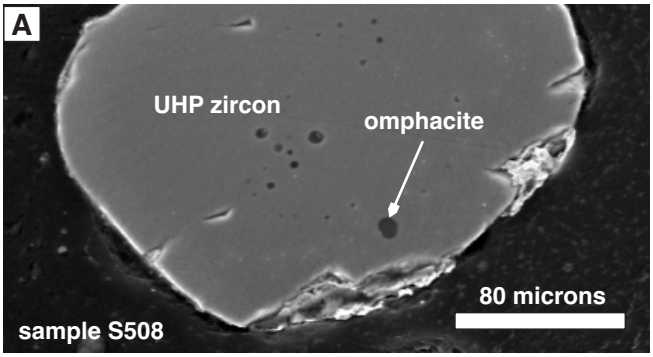

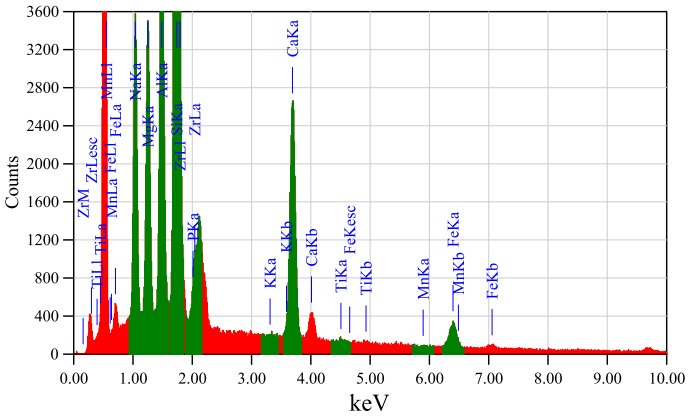

Acquisition Parameter
Instrument : 6610(LA)
Acc. Voltage : 15.0 kV
Probe Current: 1.00000 nA
PHA mode : T3
Real Time : 55.72 sec
Live Time : 50.00 sec
Dead Time : 10 %
Counting Rate: 9910 cps
Energy Range : 0 - 20 keV

ZAF Method Standardless Quantitative Analysis(Oxide)
Fitting Coefficient : 0.3768
Total Oxide : 6.0

Element	(keV)	Mass%	Error%	Mol%	Compound	Mass%	Cation	K
O		45.12						
Na K	1.041	4.95	0.50	6.62	Na2O	6.68	0.46	8.1542
Mg K	1.253	4.25	0.59	10.75	MgO	7.05	0.37	6.3516
Al K	1.486	6.29	0.69	7.16	Al2O3	11.88	0.50	10.3488
Si K	1.739	26.54	0.89	58.08	SiO2	56.78	2.01	47.9665
P K								
K K	3.312	0.07	0.86	0.06	K2O	0.09	0.00	0.1563
Ca K	3.690	8.41	1.18	12.90	CaO	11.77	0.45	19.1746
Ti K	4.508	0.20	1.92	0.26	TiO2	0.34	0.01	0.3883
Mn K	5.894	0.09	2.91	0.10	MnO	0.11	0.00	0.1607
Fe K	6.398	3.10	3.22	3.41	FeO	3.98	0.12	5.9299
Zr L	2.042	0.98	1.94	0.66	ZrO2	1.33	0.02	1.3691
Total		100.00		100.00		100.00	3.94	

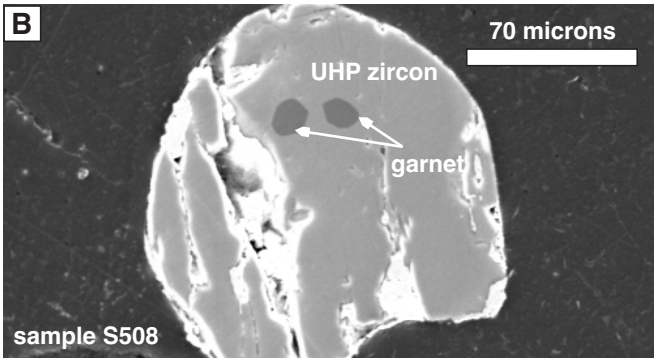

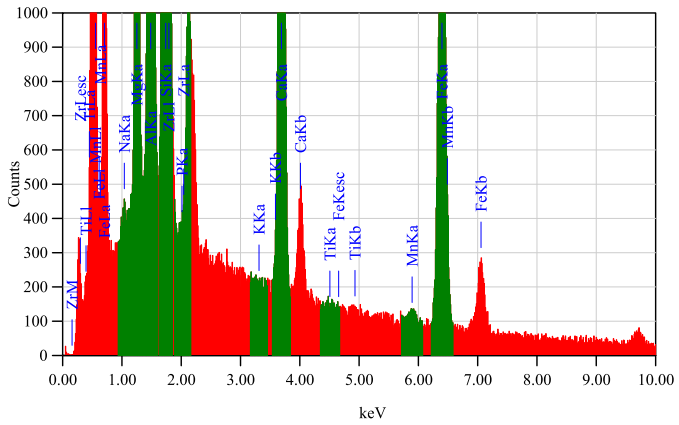

Acquisition Parameter
Instrument : 6610(LA)
Acc. Voltage : 15.0 kV
Probe Current: 1.00000 nA
PHA mode : T3
Real Time : 56.27 sec
Live Time : 50.00 sec
Dead Time : 11 %
Counting Rate: 9819 cps
Energy Range : 0 - 20 keV

ZAF Method Standardless Quantitative Analysis(Oxide)
Fitting Coefficient : 0.4123
Total Oxide : 12.0

Element	(keV)	Mass%	Error%	Mol%	Compound	Mass%	Cation	K
O		41.51						
Na K	1.041	0.09	0.64	0.13	Na2O	0.13	0.02	0.1217
Mg K	1.253	2.85	0.68	7.80	MgO	4.72	0.54	3.7354
Al K	1.486	11.61	0.77	14.32	Al2O3	21.93	1.99	17.3332
Si K	1.739	18.55	1.02	43.98	SiO2	39.69	3.06	29.5618
P K								
K K	3.312	0.02	0.91	0.01	K2O	0.02	0.00	0.0322
Ca K	3.690	7.39	1.23	12.28	CaO	10.34	0.85	16.2009
Ti K	4.508	0.07	2.00	0.10	TiO2	0.12	0.01	0.1369
Mn K	5.894	0.24	3.06	0.29	MnO	0.31	0.02	0.4280
Fe K	6.398	17.67	3.38	21.07	FeO	22.74	1.46	32.4499
Zr L								
Total		100.00		100.00		100.00	7.95	

Fig. S2